

## THE 2- AND 3-POINT CORRELATION FUNCTIONS OF THE POLARIZED 5-YEAR *WMAP* SKY MAPS

E. GJERLØW<sup>1,6</sup>, H. K. ERIKSEN<sup>2,6,7</sup>, A. J. BANDAY<sup>3,8,9</sup>, K. M. GÓRSKI<sup>4,10,11</sup> AND P. B. LILJE<sup>5,6,7</sup>

*Draft version January 3, 2019*

### ABSTRACT

We present the two- and three-point real space correlation functions of the five-year *WMAP* sky maps, and compare the observed functions to simulated  $\Lambda$ CDM concordance model ensembles. In agreement with previously published results, we find that the temperature correlation functions are consistent with expectations. However, the pure polarization correlation functions are acceptable only for the 33GHz band map; the 41, 61 and 94 GHz band correlation functions all exhibit significant large-scale excess structures. Further, these excess structures very closely match the correlation functions of the two (synchrotron and dust) foreground templates used to correct the *WMAP* data for galactic contamination, with a cross-correlation statistically significant at the  $2 - 3\sigma$  confidence level. The correlation is slightly stronger with respect to the thermal dust template than with the synchrotron template.

*Subject headings:* cosmic microwave background — cosmology: observations — methods: numerical

### 1. INTRODUCTION

Observations of the cosmic microwave background (CMB) have been among the most important ingredients in the revolution of cosmology that has taken place in the last two decades, when cosmology changed from a data starved to a data rich science. The so far most influential observations have been made with the *Wilkinson Microwave Anisotropy Probe* (*WMAP*; Bennett et al. 2003; Hinshaw et al. 2007, 2009) satellite experiment, which has measured the microwave sky at five different frequencies (23, 33, 41, 61 and 94 GHz) in both temperature and polarization. Its main results are five sky maps with resolutions between  $13'$  and  $55'$ , each comprising more than three million pixels in each of the three Stokes parameters I, Q and U.

Almost as important as the progress in detector technology leading to instruments like *WMAP*, has been the progress in computer technology and algorithms. With the enormously increased number of pixels from new high resolution instruments, scientists have had to develop clever algorithms for every step of the required data analysis pipeline; map-making (e.g., Ashdown et al. 2007; Hinshaw et al. 2003b and references therein), component separation (e.g., Bennett et al. 2003; Leach et al. 2008; Eriksen et al. 2008 and references therein), power spectrum and cosmological parameter estimation (e.g., Górski 1994; Lewis & Bridle 2002; Hivon et al. 2003;

Hinshaw et al. 2003a; Verde et al. 2003; Eriksen et al. 2004d and references therein), and analysis of higher-order statistics (e.g., Hinshaw et al. 1994; Kogut et al. 1995; Komatsu et al. 2003; Eriksen et al. 2004b, 2005 and references therein).

In this paper, we revisit a well-known example of the latter category, namely real-space  $N$ -point correlation functions. These functions arise naturally in studies of non-Gaussianity, since it can be shown that any odd-ordered  $N$ -point function has an identically vanishing expectation value, while all even-ordered  $N$ -point functions have an expectation value given by products of the corresponding 2-point functions. Violation of either of these relations would indicate the presence of a non-Gaussian component in the field under consideration.

Earlier  $N$ -point correlation function analyses of CMB data include studies of the COBE-DMR data (Hinshaw et al. 1995; Kogut et al. 1996; Eriksen et al. 2002), the *WMAP* temperature data (Eriksen et al. 2005) and one single two-point analysis of the first-year *WMAP* polarization data (Kogut et al. 2003). This paper is the first to consider the much more mature 5-year *WMAP* polarization data, and the first to compute the 3-point correlation function from any CMB polarization data. To do this, we adopt and extend the  $N$ -point algorithms developed by Eriksen et al. (2004c).

### 2. METHODS AND DEFINITIONS

#### 2.1. $N$ -point correlation functions

An  $N$ -point correlation function  $C_N$  of a stochastic field  $X(\hat{n})$  is defined as

$$C_N(\theta_1, \theta_2, \dots, \theta_k) = \left\langle X(\hat{n}_1)X(\hat{n}_2) \cdots X(\hat{n}_N) \right\rangle, \quad (1)$$

where  $\{\hat{n}_1, \dots, \hat{n}_N\}$  spans an  $N$ -polygon defined by  $k$  parameters,  $\{\theta_1, \dots, \theta_k\}$ . In the most general case in which no assumptions are made concerning the statistical properties of the field  $X$ , one needs  $k = 2N$  parameters to

<sup>1</sup> Electronic address: eirik.gjerlow@astro.uio.no

<sup>2</sup> Electronic address: h.k.k.eriksen@astro.uio.no

<sup>3</sup> Electronic address: Anthony.Banday@cesr.fr

<sup>4</sup> Electronic address: Krzysztof.M.Gorski@jpl.nasa.gov

<sup>5</sup> Electronic address: per.lilje@astro.uio.no

<sup>6</sup> Institute of Theoretical Astrophysics, University of Oslo, P.O. Box 1029 Blindern, N-0315 Oslo, Norway

<sup>7</sup> Centre of Mathematics for Applications, University of Oslo, P.O. Box 1053 Blindern, N-0316 Oslo

<sup>8</sup> Centre d'Etude Spatiale des Rayonnements 9, av du Colonel Roche, BP 44346 31028 Toulouse Cedex 4, France

<sup>9</sup> Max-Planck Institute für Astrophysik, Karl-Schwarzschild Str. 1, D-85748, Garching, Germany

<sup>10</sup> JPL, M/S 169/327, 4800 Oak Grove Drive, Pasadena CA 91109

<sup>11</sup> Warsaw University Observatory, Aleje Ujazdowskie 4, 00-478 Warszawa, Poland

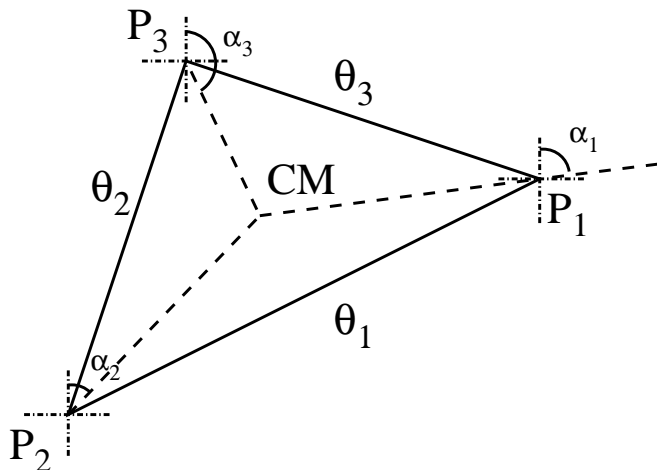


FIG. 1.— The center of mass and rotation angles of a triangle. Each point  $i$  is rotated by an angle  $\alpha_i$  from the global coordinate system into the local system defined by the triangle’s center of mass.

uniquely describe such a polygon<sup>12</sup>, namely the individual positions of each vertex of the polygon. However, in many applications one assumes that  $X$  is isotropic and homogeneous, and one can therefore average over position. In such cases, the number of parameters are reduced by 3 on a two-dimensional surface, corresponding to translation and rotation.

In this paper, we will consider only 2- and 3-point correlation functions defined on the two-dimensional sphere, and we therefore need respectively 1 and 3 parameters to describe our polygons (ie., line and triangle). In the 2-point case, the only natural parameter choice is the angular distance,  $\theta = \arccos(\hat{n}_1 \cdot \hat{n}_2)$  between the two points, while in the 3-point case there is some freedom to choose. For simplicity, we parameterize the triangle by the lengths of the three edges,  $(\theta_1, \theta_2, \theta_3)$ , where the edges are ordered such that  $\theta_1$  corresponds to the longest of the three edges, and the remaining are listed according to clockwise traversal of the triangle.

## 2.2. Polarized correlation functions

Our goal in this paper is to measure the  $N$ -point correlation functions of the polarized *WMAP* maps. To do so, we have to generalize the methods described by Eriksen et al. (2004c), in order to account for the fact that the CMB polarization field is a spin-2 field. Explicitly, the full CMB fluctuation field may be described in terms of the three Stokes parameters,  $I(\hat{n})$ ,  $Q(\hat{n})$ , and  $U(\hat{n})$ . Here  $I$  is the usual (scalar) temperature fluctuation field, and  $Q$  and  $U$  are two parameters describing the linear polarization properties of the radiation in direction  $\hat{n}$ .

According to standard CMB conventions,  $Q$  and  $U$  are defined with respect to the local meridian of the spherical coordinate system of choice. However,  $Q$  and  $U$  form a spin-2 field, and this means that if one performs a rotational coordinate system transformation, the Stokes parameters after transformation becomes

$$\begin{pmatrix} I' \\ Q' \\ U' \end{pmatrix} = \begin{pmatrix} 1 & 0 & 0 \\ 0 & \cos 2\alpha & \sin 2\alpha \\ 0 & -\sin 2\alpha & \cos 2\alpha \end{pmatrix} \begin{pmatrix} I \\ Q \\ U \end{pmatrix}, \quad (2)$$

<sup>12</sup> In this paper, we restrict our interest to fields defined on the two-dimensional sphere.

where  $\alpha$  is the local rotation angle between the two coordinate systems. Zaldarriaga & Seljak (1997) and Kamionkowski et al. (1997) give complete descriptions of the statistics of these fields.

This property has some important consequences when computing  $N$ -point correlation functions: Since we assume that the CMB field is isotropic and homogeneous, the value we obtain for a given element of the correlation function should not depend on the coordinate system. One can therefore not blindly adopt  $Q$  and  $U$  as the quantities to correlate, since these are in fact coordinate dependent.

For the two-point function, this problem is conventionally solved by defining a local coordinate system in which the local meridian passes through the two points of interest (Kamionkowski et al. 1997). The Stokes parameters in this new “radial” system are denoted  $Q^r$  and  $U^r$ , and measure the polarization either orthogonally or perpendicularly ( $Q^r$ ) to the connecting line, or  $45^\circ$  rotated with respect to it ( $U^r$ ). The two-point function defined in terms of  $Q^r$  and  $U^r$  then becomes coordinate system independent.

We now generalize this idea to higher-order  $N$ -point correlation functions. As with the definition of the  $N$ -point polygon parameters, we also here have some freedom when choosing the reference points for the coordinate independent quantities. For instance, two natural choices for  $Q_i^r$  and  $U_i^r$  are to define them either with respect to the edges or with respect to the center of mass of the polygon,

$$\hat{n}_{CM} = \frac{\sum_i \hat{n}_i}{|\sum_i \hat{n}_i|}. \quad (3)$$

In this paper we choose the latter definition. The resulting geometry is illustrated in Figure 1.

Given these new rotationally invariant quantities,  $X \in \{I, Q^r, U^r\}$ , defined with respect to the local center of mass, the polarized correlation functions are simply defined as

$$C_N(\theta_1, \theta_2, \dots, \theta_k) = \left\langle X_1(\hat{n}_1) X_2(\hat{n}_2) \cdots X_N(\hat{n}_N) \right\rangle, \quad (4)$$

Note that in the case of the two-point function, there are six independent polarized correlation functions (II,  $IQ^r$ ,  $IU^r$ ,  $Q^r Q^r$ ,  $Q^r U^r$  and  $U^r U^r$ ), while in the three-point function case, there are 27 independent components (III,  $IIQ^r$ , ...,  $U^r U^r Q^r$ ,  $U^r U^r U^r$ ).

Algorithmically, we compute these functions from a given pixelized sky map,  $m(\hat{n})$ , simply by averaging the corresponding products over all available pixel multiplets that satisfy the geometrical constraints of the polygon under consideration,

$$\hat{C}_N(\theta_1, \theta_2, \dots, \theta_k) = \frac{1}{N_p} \sum_i^{N_p} m_{p_1(i)}^{X_1} m_{p_2(i)}^{X_2} \cdots m_{p_N(i)}^{X_N}. \quad (5)$$

Here  $i = 1, \dots, N_p$  runs over the number of available pixel multiplets, and  $p_j(i)$  is the  $j$ ’th pixel in the  $i$ ’th pixel multiplet. For full details on how to find the relevant pixel multiplets corresponding to a given polygon efficiently, see Eriksen et al. (2004c).

The correlation functions are binned with a bin size tuned to the pixel size of the map. Explicitly, since we use

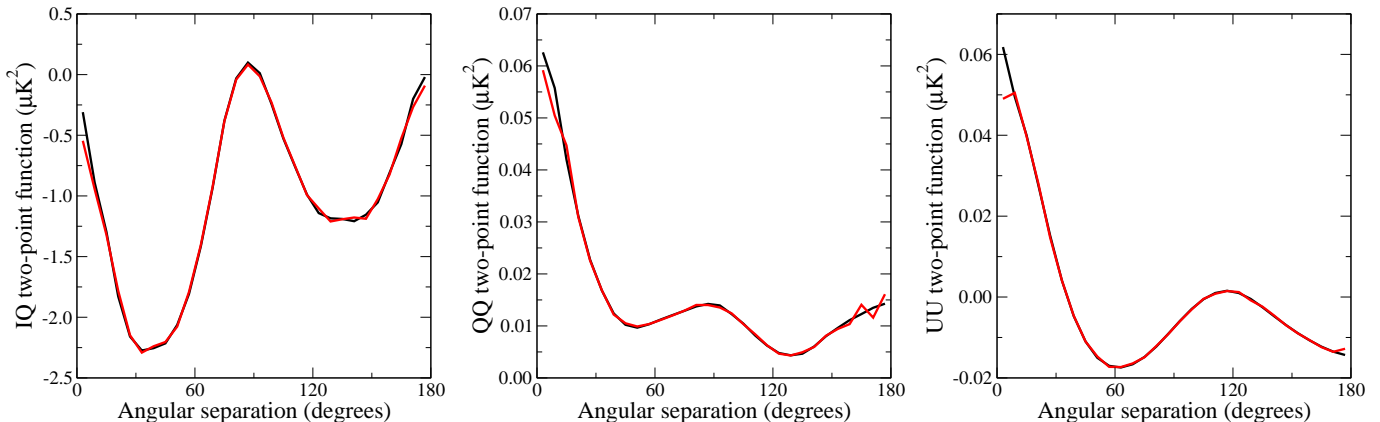


FIG. 2.— Comparison between the analytically calculated two-point function (black) and the two-point function computed from the map with the corresponding  $C_l$ 's (red). The shown functions are, from left to right, the IQ, QQ and UU correlation functions.

a HEALPix resolution of  $N_{\text{side}} = 16$ , with  $\sim 3^\circ$  pixels, we adopt a bin size of  $6^\circ$ , for a total of 30 bins between 0 and  $180^\circ$ .

If all factors in an N-point multiplet are taken from the same map, the resulting function is named an auto-correlation; otherwise it is called a cross-correlation. The main advantage of cross-correlations is that the noise is typically uncorrelated between maps, while the signal (ideally) is strongly correlated. Therefore, the noise contribution to a cross-correlation averages to zero. For this reason, one typically uses auto-correlations as a probe of systematic errors (e.g., to check whether the assumed noise model is correct), but cross-correlations for a final cosmological analysis. In this paper, we consider both types.

In Figure 2, we show a comparison of three 2-point correlation functions computed from the same signal-only simulation, using two different methods: The red curves show the correlation functions computed from the power spectrum of the realization, employing the analytic expression given by, e.g., Smith (2006). The black curves show the correlation functions computed directly from the pixelized map using the algorithms described above. Slight differences are expected due to different treatment of pixel windows, but clearly the agreement between the two are excellent, giving us confidence that our machinery works as expected.

### 2.3. Comparison with simulations

In this paper we perform a standard frequentist analysis, in the sense that we compare the results obtained from the real data with an ensemble of simulations based on some model. Specifically, our null-hypothesis here is that the universe is isotropic and homogeneous, and filled with Gaussian fluctuations drawn from a  $\Lambda$ CDM power spectrum. Our ensemble consists of  $N_{\text{sim}} = 100\,000$  simulations.

For each realization in the ensemble, we compute the N-point correlation functions in precisely the same manner as for the real data. Finally, we compare the correlation function derived from the data with the simulated functions through a standard  $\chi^2$  statistic,

$$\chi^2 = \sum_{b=1}^{N_{\text{bin}}} \frac{(C(b) - \mu(b))^2}{\sigma_b^2}, \quad (6)$$

where the sum runs over all N-point configurations/bins, and the mean  $\mu(b) = \langle C(b) \rangle$  and variance  $\sigma^2(b) = \langle (C(b) - \mu(b))^2 \rangle$  are derived from the simulations.

However, before computing the  $\chi^2$  as described above, we Gaussianize the distribution of each bin as follows (Eriksen et al. 2005),

$$\frac{R}{N_{\text{sim}} + 1} = \frac{1}{\sqrt{2\pi}} \int_{-\infty}^s e^{-\frac{1}{2}t^2} dt, \quad (7)$$

where  $R$  is the rank of the value under consideration (i.e., the number of simulations with a *lower* value than the currently considered), and  $s$  is the corresponding Gaussianized rank. The reason for performing this transformation is that the probability distribution for a given bin is highly non-Gaussian, and for even-ordered correlation functions strongly skewed towards high values. A direct  $\chi^2$  evaluation will therefore tend to give too much weight to fluctuations that have high values compared to fluctuations that have low values. By first explicitly Gaussianizing, a symmetric response is guaranteed.

The final results are quoted as the fraction of simulations with a *higher*  $\chi^2$  than the real data. By splitting the simulations into two disjoint sets, and repeating the  $\chi^2$  analysis for each set, we estimate that the Monte Carlo uncertainty in the resulting significances is less than 1%. For this reason, we quote cases inconsistent with simulations at more than 99% by instead providing the actual number of simulations with higher  $\chi^2$ . This allows us to distinguish between a case with  $\sim 1\%$  significance and one with  $\sim 0.1\%$  significance, but still recognize the importance of the Monte Carlo uncertainties. Further, we conservatively never claim to obtain results with higher significance than 99% in any case, despite the fact that many results very likely are far more anomalous, as would be clear by using more simulations.

### 3. DATA AND SIMULATIONS

In the following, we analyze the 5-year WMAP sky maps, including both temperature and polarization. These data are available from LAMBDA<sup>13</sup>, including all ancillary data, such as beam transfer functions, noise covariance matrices and foreground templates. The total

<sup>13</sup> <http://lambda.gsfc.nasa.gov>

TABLE 1  
STATISTICAL SIGNIFICANCES (TWO-POINT FUNCTIONS)

Frequency	Correlation									
	II	IQ	IU	QI	QQ	QU	UI	UQ	UU	
KQ85										
<i>KaxKa</i>	—	—	—	—	0.40 (0.32)	0.45 (0.38)	—	...	0.32 (0.25)	
<i>QxQ</i>	0.08	0.85	0.65	...	0.01 (348*)	0.01 (0.01)	...	...	254* (128*)	
<i>QxV</i>	0.07	0.26	0.61	0.85	25* (18*)	0.06 (0.04)	0.69	0.01 (338*)	0.04 (0.02)	
<i>QxKa</i>	—	0.81	0.97	—	0.01 (307*)	0.02 (0.01)	—	0.03 (0.02)	154* (48*)	
<i>QxW</i>	0.08	0.84	0.05	0.86	3* (5*)	0* (0*)	0.69	0* (0*)	253* (222*)	
<i>VxV</i>	0.07	0.27	0.60	...	73* (49*)	0.02 (0.01)	...	...	0.01 (393*)	
<i>VxKa</i>	—	0.82	0.97	—	0.01 (357*)	21* (15*)	—	18* (10*)	0.02 (0.02)	
<i>VxW</i>	0.07	0.84	0.05	0.27	1* (2*)	42* (14*)	0.57	37* (8*)	106* (88*)	
<i>WxKa</i>	—	0.78	0.98	—	—	—	—	—	—	
<i>WxW</i>	0.07	0.83	0.05	...	3* (0*)	71* (34*)	...	...	2* (0*)	
<i>W1xW1</i>	0.09	0.70	0.11	...	116* (123*)	0.01 (0.01)	...	...	5* (6*)	
<i>W2xW2</i>	0.07	0.32	0.22	...	95* (83*)	0.03 (0.03)	...	...	478* (476*)	
<i>W3xW3</i>	0.07	0.91	0.82	...	0.78 (0.78)	0.94 (0.94)	...	...	0.60 (0.60)	
<i>W4xW4</i>	0.10	0.53	0.03	...	0* (0*)	0.08 (0.08)	...	...	1* (3*)	
KQ75										
<i>QxQ</i>	0.07	0.96	0.61	...	...	...	...	...	...	
<i>QxV</i>	0.06	0.30	0.67	0.97	...	...	0.62	...	...	
<i>QxKa</i>	—	0.87	0.95	—	...	...	—	...	...	
<i>QxW</i>	0.06	0.91	0.15	0.97	...	...	0.64	...	...	
<i>VxV</i>	0.06	0.31	0.65	...	...	...	...	...	...	
<i>VxKa</i>	—	0.88	0.96	—	...	...	—	...	...	
<i>VxW</i>	0.06	0.92	0.16	0.32	...	...	0.62	...	...	
<i>WxKa</i>	—	0.85	0.96	—	...	...	—	...	...	
<i>WxW</i>	0.06	0.92	0.15	...	...	...	...	...	...	
<i>W1xW1</i>	0.08	0.68	0.16	...	...	...	...	...	...	
<i>W2xW2</i>	0.06	0.33	0.35	...	...	...	...	...	...	
<i>W3xW3</i>	0.06	0.93	0.94	...	...	...	...	...	...	
<i>W4xW4</i>	0.10	0.57	0.10	...	...	...	...	...	...	

NOTE. — Statistical significances for the two-point functions as computed from the *WMAP* data. For the *W* differencing assemblies, the first year maps were used. For the band data, the 5-year co-added maps were used. The Monte Carlo uncertainty is 1%. The correlations using both the KQ85 and the KQ75 mask are shown. As the pure polarization correlations are insensitive to which I mask is being used, these are only displayed under the KQ85 header. An entry with '...' signifies that some other entry in the table contains the same information as that entry, while an entry with '—' indicates that the information in that entry was not computed. The listed ratios indicate the fraction of simulations with a higher  $\chi^2$  than the observed data. The entries marked with a '\*' signifies that the fraction is lower than the Monte Carlo uncertainty, but still larger than zero; consequently, the number of simulations (out of 100,000) with a higher  $\chi^2$  than the observed data are shown instead for these entries. The entries in parenthesis are the significances of the noise-only hypothesis.

data set spans five frequencies (23, 33, 41, 61 and 94 GHz), corresponding to the *K*, *Ka*, *Q*, *V* and *W* bands.

Our main objects of interest are the frequency co-added and foreground-reduced sky maps, which are provided in the form of HEALPix<sup>14</sup> pixelized sky maps. The temperature sky maps are given at a HEALPix resolution of  $N_{\text{side}} = 512$ , while the polarization maps are given at  $N_{\text{side}} = 16$ . To bring the data into a common format, we therefore degrade the temperature component to the same resolution as the polarization maps, simply by averaging over sub-pixels in a low-resolution pixel.

For temperature we consider the *Q*-, *V*- and *W*-bands, and for polarization also the *Ka*-band. This difference mirrors the official cosmological *WMAP* analysis, which also uses the *Ka*-band for polarization, but considers the same band to be too foreground contaminated in temperature.

Our simulations are generated as follows: We first draw a random Gaussian CMB realization from the best-fit 5-year *WMAP*  $\Lambda$ CDM power spectrum, including multipole moments up to  $\ell_{\text{max}} = 1024$ . This realization is then convolved with the instrumental beam of each *WMAP* differencing assembly and the  $N_{\text{pix}} = 512$  HEALPix pixel

window, and projected onto a HEALPix grid. For temperature, we then add a Gaussian noise realization with pixel-dependent variance,  $\sigma_p^2 = \sigma_0^2/N_{\text{obs}}(p)$ , where  $\sigma_0^2$  is the noise variance per observation and  $N_{\text{obs}}$  is the number of observations in that given pixel. The temperature component is then degraded to  $N_{\text{side}} = 16$ .

For the polarization component, we first degrade the high-resolution map to  $N_{\text{side}} = 16$ , and then add a noise term. This is because the polarized noise description for *WMAP* is given by a full noise covariance matrix,  $\mathbf{C}_{p,p'}$  at  $N_{\text{side}} = 16$ , and not as a simple  $N_{\text{obs}}$  count at high resolution. The correlated noise realization is generated by drawing a vector of standard normal variates,  $\eta \sim N(0, 1)$ , and multiplying this vector by the Cholesky factor of the covariance matrix,  $\mathbf{n} = \mathbf{L}\eta$ , where  $\mathbf{C} = \mathbf{L}\mathbf{L}^t$ .

For temperature, we adopt two different masks, namely the 5-year *WMAP* KQ85 and KQ75 masks. These exclude 18 and 28% of the sky, respectively. For the polarization component, there is only one relevant mask in the 5-year *WMAP* data release, which excludes 27% of the sky.

Two different polarized foreground templates are used in the following. The first is simply the difference between the *K* and *Ka* bands, smoothed to an effective res-

<sup>14</sup> <http://healpix.jpl.nasa.gov>

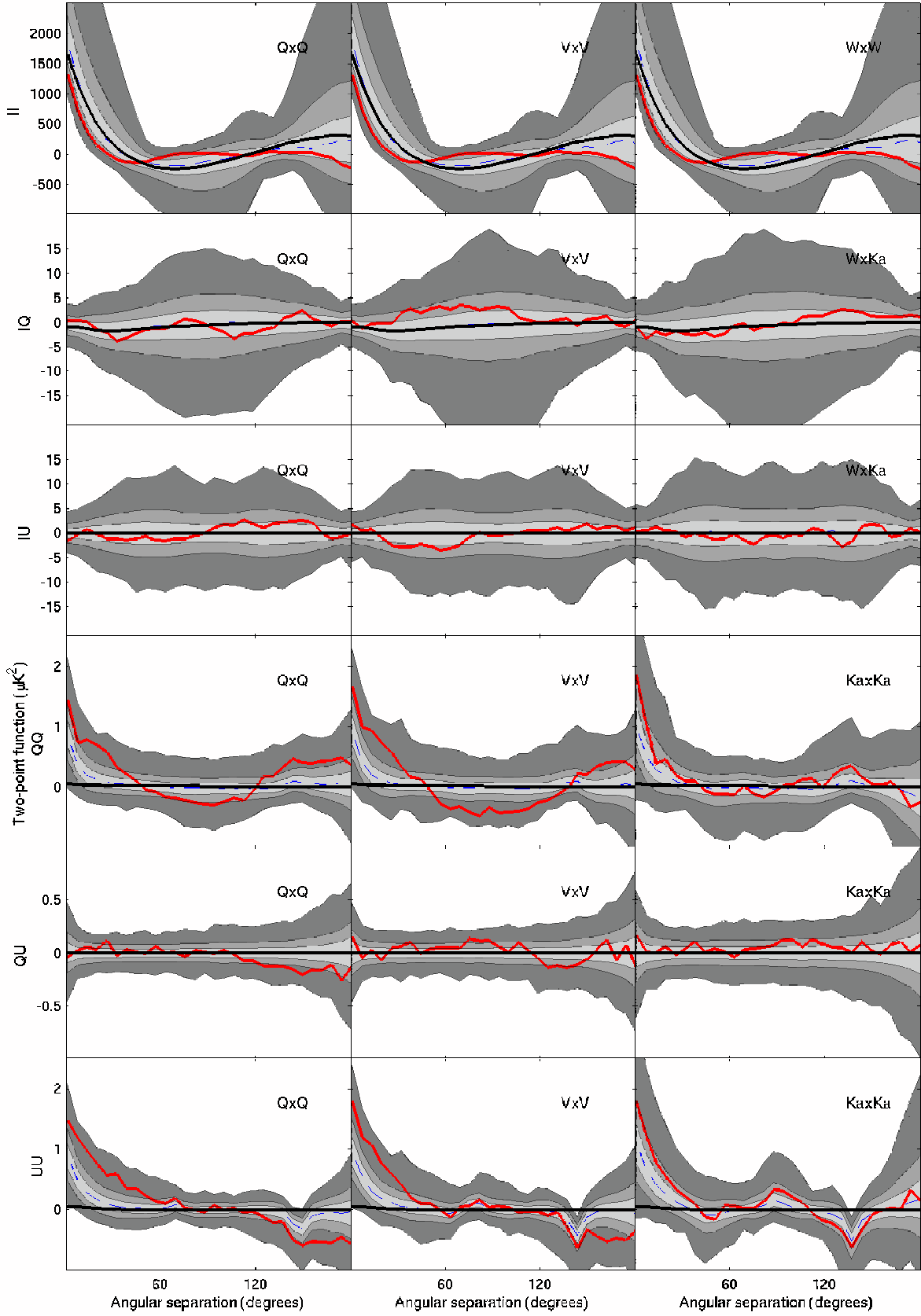


FIG. 3.— Two-point functions computed with the KQ85 mask, as functions of angular separation on the sky. Only the  $Ka$ ,  $Q$  and  $V$  auto-correlations, as well as the cross-correlations between the  $W$  intensity map and the  $Ka$  polarization map, are shown. The red line shows the two-point function computed from the *WMAP* 5-year co-added maps. The light, medium and dark grey shaded areas correspond to  $1\sigma$ ,  $2\sigma$ , and  $3\sigma$ , respectively. The dashed blue line is the maximal point of the correlation histograms, while the black line is the theoretically predicted (no noise) two-point function computed from the best-fit 5-year *WMAP*  $\Lambda$ CDM power spectrum. Each row corresponds to a specific combination of modes, while the frequency bands involved are marked on each plot.

olution of  $10^\circ$  to reduce noise, which traces synchrotron radiation. The second template is the same starlight template as used for foreground correction in the 5-year *WMAP* data release, which traces thermal dust.

#### 4. RESULTS

In this section we present the two- and three-point correlation functions computed from the polarized 5-year *WMAP* data. Due to the large number of available and unique correlation functions one can form within this data set, we plot only a few selected cases, and instead show the full set of results only in the form of tabulated significances.

##### 4.1. Two-point correlations

In Figure 3 we show a selection of two-point correlation functions derived from the *WMAP* data. Specifically, all available *Ka*, *Q* and *V* auto-correlations are shown, in addition to the cross-correlations between the *Ka* and *W* bands. Table 1 shows the  $\chi^2$  significances for all possible two-point functions from the available data. (Note that only unique combinations are actually shown; empty table cells indicates that the same combinations may be found elsewhere in the table. For example, IQ and QI are identical for auto-correlations, but different for cross-correlations.)

Starting with the pure intensity correlations shown in the top row of Figure 3, we recognize the by now well-known behavior of the CMB temperature two-point function, observed both by COBE (e.g., Bennett et al. 1994) and *WMAP* (e.g., Spergel et al. 2003): At small angular separations, it is slightly low compared to the  $\Lambda$ CDM model, and at separations larger than  $60^\circ$ , very close to zero. This peculiar behavior has attracted the interest of both experimentalists and theorists, and some have suggested that this could be the signature of a closed topological space. However, from the view of a simple  $\chi^2$  test, this function remains consistent with the simplest  $\Lambda$ CDM model at the 5–10% level.

Next, looking at the temperature-polarization (I-Q/U) cross-correlations we see that the overall behavior of the *Q*-, *V* and *Ka*  $\times$  *W* band functions are quite different. This indicates that the *WMAP* data still are too noise dominated to extract high-sensitivity cosmological information from individual bands. This is also reflected in the second and third columns of Table 1, where there is a significant scatter between the different results. However, we do see that all results are in good agreement with the expectations, indicating that the noise model is satisfactory.

The three bottom rows of Figure 3 show the pure polarization correlation functions, which are the main target in this paper. And here we see several interesting features. First, we recognize a sharp feature in the UU correlation function at  $\sim 141^\circ$ . This is the angular separation between the A- and B-sides of the differential *WMAP* detectors, and it was also seen in the pure noise temperature two-point correlation function in the first-year *WMAP* data (Eriksen et al. 2005).

However, even more interesting is the overall very pronounced large-scale excesses seen in the QQ and UU functions: Both the *Q*- and *V*-band functions lie mostly within the  $2\text{--}3\sigma$  confidence regions, and the overall agreement with the simulations appears quite poor.

Again, this is strongly reflected in Table 1: All QQ correlations are anomalous at more than 99% confidence, and all UU correlations at more than 98% confidence. In the case of the *W*-band, which happens to be the most anomalous of any band, we have good reasons to expect such behavior. This band has a significantly higher  $1/f$  knee frequency than any other band (Jarosik et al. 2003), with the *W4* differencing assembly having the highest. As a result, the *WMAP* team has chosen not to use this band for cosmological analysis in polarization. But the anomalous behavior of the *Q* and *V* bands is *a priori* not expected; these are used for cosmological analysis by the *WMAP* team, and should be clean.

We have also generated an ensemble of noise-only simulations, and computed the two-point functions from these. The corresponding  $\chi^2$  fractions are listed in parentheses in Table 1 for the pure polarization modes. Here we see that, generally speaking, the noise-only hypothesis performs almost, but not quite, as well as the signal plus noise hypothesis. This is simply due to the fact that the *WMAP* polarization data are strongly dominated by the correlated noise, and it is very difficult from a correlation function point-of-view to distinguish between a small signal component and a large-scale noise fluctuation.

##### 4.1.1. Foreground cross-correlations

The anomalous behavior seen in the *Q*- and *V*-band two-point functions clearly needs an explanation. And typically, when such unexpected behavior is observed, one of the the first issues to consider is residual foregrounds.

To check whether this may be a relevant issue, we first simply compute the cross-correlation functions between each of the three frequency bands (*Ka*, *Q* and *V*) and the two available foreground templates (synchrotron and dust). This is done both for the real *WMAP* data and the simulated ensembles, and the agreement between the (pure CMB + noise) simulations and the *WMAP* data is again quoted in terms of a  $\chi^2$  fraction.

The results from these calculations are as follows: For the *Ka*-band, we find that the  $\chi^2$  significances are 0.51 and 0.24 for synchrotron and dust respectively, indicating no significant foreground detection in this case. However, for the *Q*-band the corresponding numbers are 0.05 and  $\sim 0.005$ , corresponding to correlations statistically significant at 2 and  $\sim 3\sigma$ , respectively. For the *V*-band, the numbers are 0.05 and 0.02, significant at  $2\sigma$  or more.

To study these foreground correlations further, we compute the two-point functions from the foreground templates directly, and fit these to the observed correlation functions with a single free amplitude for each template,  $A_s$  and  $A_d$ , by minimizing

$$\chi_{\text{fg}}^2 = \sum_{bb'} (C_{\text{obs}}(b) - C_{\text{sim}}(b) - A_s C_s(b) - A_d C_d(b)) \Sigma_{\text{sim}}^{-1}(b, b') \times (C_{\text{obs}}(b') - C_{\text{sim}}(b') - A_s C_s(b') - A_d C_d(b')).$$

Here  $C_{\text{sim}}(b)$  is the correlation function mean and  $\Sigma_{\text{sim}}(b, b') = \langle (C(b) - \mu(b))(C(b') - \mu(b')) \rangle$  is the covariance matrix, both quantities obtained from the noise simulations. The indices  $b, b'$  runs over all possible pure polarization two-point bins (i.e., both angular bins and QQ, QU and UU correlations).

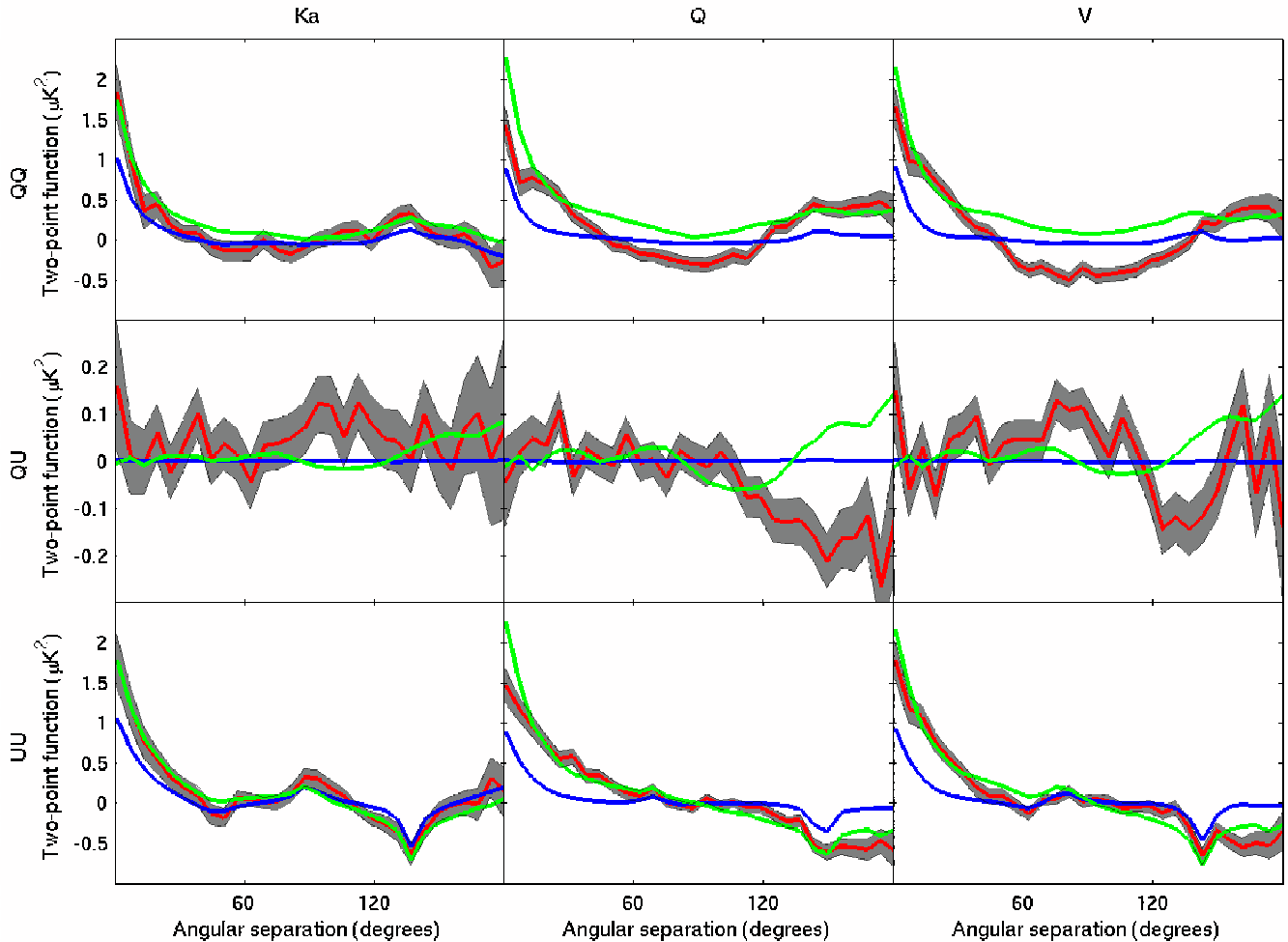


FIG. 4.— The template two-point functions fitted to the *WMAP* data two-point functions. The red line shows the *WMAP* data, with the gray area being the  $1\sigma$  confidence intervals. The blue line shows the the mean correlation function of the simulations, while the green line shows the mean value plus the foreground contribution.

TABLE 2  
AMPLITUDE CONFIDENCE INTERVALS

Band	Synchrotron		Dust	
	$A_s$	$\sigma_{sig}$	$A_d$	$\sigma_{sig}$
<i>Ka</i>	$0.0038 \pm 0.0013$	2.9	$0.0115 \pm 0.0057$	2.0
<i>Q</i>	$0.0052 \pm 0.0010$	5.2	$0.0256 \pm 0.0042$	6.1
<i>V</i>	$0.0063 \pm 0.0011$	5.7	$0.0197 \pm 0.0047$	4.2

NOTE. — Mean values and confidence intervals for the best-fit amplitudes of the  $K-Ka$  and dust template two-point functions relative to the *WMAP* data two-point functions.

The resulting best-fit amplitudes from this calculation for *Ka*-, *Q*- and *V*-bands are shown in Table 2. Here we again see that the *Ka*-band amplitudes are generally significantly lower than those of the *Q*- and *V*-bands. (Note that the uncertainties quoted in this table only include statistical errors, not systematic errors. The significances should therefore not be considered as true detection levels, but are only suggestive.)

In Figure 4 the fitted correlation functions are compared to the observed functions. First, the red curve shows the functions derived from the actual *WMAP* data, with gray bands indicating the  $1\sigma$  uncertainties derived from simulations. The blue curve shows the mean cor-

relation function of the simulations,  $C_{sim}(b)$ , and finally, the green curve shows the same, but with the foreground contribution added in,  $C_{fg}(b) = C_{sim}(b) + A_s C_s(b) + A_d C_d(b)$ . Clearly, the latter matches the real data far better than the pure CMB plus noise hypothesis, with the best match seen in the UU correlation function.

#### 4.2. Three-point correlations

We now turn to the three-point correlation functions derived from the 5-year polarized *WMAP* data. However, we note that the three-point function is primarily used in the literature as a test of non-Gaussianity. In the present case, this will not be case, since we have already seen that the data appear to be foreground contaminated, and even the two-point correlation function fails a standard  $\chi^2$  test. The following three-point analysis will therefore essentially only be a consistency check of the above results, and a demonstration of the general procedure, to be further developed in the future, when cleaner data become available.

We consider only cross-correlations of pure polarization modes for the cosmologically interesting frequency channels. This leaves us with only eight independent correlation function modes (QQQ, QUQ, UQQ, UUU etc.), and only one frequency combination (*Ka* x *Q* x *V*). Fur-

TABLE 3  
THREE-POINT FUNCTION RESULTS

Frequency	Correlation							
	QQQ	QQU	QUQ	QUU	UQQ	UQU	UUQ	UUU
Equilateral functions								
$KaxQxV$	0.04 (0.03)	0.31 (0.26)	18* (4*)	0.04 (0.03)	0.16 (0.13)	0.01 (416*)	0.07 (0.05)	0.21 (0.17)
$KaxVxQ$	0.45 (0.40)	0.10 (0.08)	0.07 (0.05)	0.01 (446*)	359* (241*)	0.35 (0.31)	0.01 (0.01)	0.11 (0.09)
Collapsed functions								
$KaxQxV$	0.49 (0.45)	0.01 (0.01)	0.23 (0.18)	0.03 (0.02)	0.63 (0.56)	0.01 (384*)	0.21 (0.18)	0.43 (0.38)
$KaxVxQ$	323* (240*)	0.01 (0.01)	2* (1*)	0.05 (0.03)	0* (1*)	0.11 (0.09)	0.05 (0.03)	17* (11*)
$QxKaxV$	0.01 (0.01)	0.28 (0.25)	0.01 (329*)	0.17 (0.14)	0.01 (298*)	231* (179*)	0.07 (0.05)	0.15 (0.12)
$QxVxKa$	0.05 (0.04)	0.09 (0.07)	0.01 (0.01)	0.10 (0.08)	0.04 (0.03)	0.07 (0.06)	0.12 (0.09)	0.12 (0.09)
$VxKaxQ$	0.21 (0.17)	0.04 (0.03)	180* (5*)	0* (2*)	3* (2*)	127* (79*)	80 (45*)	0.01 (456*)
$VxQxKa$	0.01 (0.01)	0.03 (0.02)	0.58 (0.51)	439* (301*)	0.01 (0.01)	0.38 (0.33)	0.18 (0.13)	0.05 (0.04)

NOTE. — Statistical significances of the polarization-only three-point functions computed from the *WMAP* 5-year co-added  $Ka$ ,  $Q$  and  $V$  maps. The Monte Carlo uncertainty is 1%. See table 1 for feature explanation.

ther, we consider only two general types of three-point configurations, namely equilateral and pseudo-collapsed triangles. The latter is defined such that two legs of the triangle are of equal length, while the third leg spans an angular distance of less than  $12^\circ$ .

The results from these calculations are tabulated in Table 3, and a few arbitrarily chosen modes of the equilateral three-point functions are plotted in Figure 5. (Plotting all functions would take too much space, without adding any particular new insights.)

Once again, we see that the  $\chi^2$ 's obtained from the real data are high, but generally not quite as striking as in the two-point case. This is at least partly due to the fact that the  $Ka$  band is involved in all configurations, as well as the fact that the three-point function is always “noisier” than the two-point function. We also see that the noise-only hypothesis always has higher  $\chi^2$ 's than the signal-plus-noise hypothesis, again following the two-point behavior.

It is difficult to interpret these results much further, given that there are clear problems already at the two-point level. We therefore leave a full interpretation of the three-point function to a future publication, when cleaner data, either from *WMAP* or *Planck*, have been made available.

## 5. CONCLUSIONS

We compute for the first time the polarized two- and three-point correlation functions from the 5-year *WMAP* data, with the initial motivation of constraining possible non-Gaussian signals on large scales in the CMB polarization sector. However, our main result is a detection of a signature consistent with residual foregrounds in both the  $Q$ - and  $V$ -band data, significant at  $2-3\sigma$ .

<sup>15</sup> <http://www.eso.org/science/healpix/>

This should not come as a complete surprise, though, as a similar result was found in the 3-year *WMAP* data through a direct template fit approach by Eriksen et al. (2007). They used a Gibbs sampling implementation to estimate the joint CMB power spectrum and foreground template posterior, and found non-zero template amplitudes at similar significance levels when marginalizing over the CMB spectrum. Given the results found in the present paper, this still appears to be an important issue for the 5-year *WMAP* data release. Resolving this question is of major importance for the CMB community, since many cosmological parameters depend critically on the large-scale *WMAP* polarization data, most notably the optical depth of reionization,  $\tau$ , and the spectral index of scalar perturbations,  $n_s$ .

The question of primordial non-Gaussianity in CMB polarization data can not be meaningfully addressed as long as this issue is unresolved. The three-point correlation function results shown in this paper therefore mostly serves as a demonstration of the approach, and as a cross-check on the two-point results. The three-point function will obviously become a more important and independent quantity in the future, when higher-fidelity polarization data become available.

We acknowledge use of the HEALPix<sup>15</sup> software (Górski et al. 2005) and analysis package for deriving the results in this paper, and use of the Legacy Archive for Microwave Background Data Analysis (LAMBDA). HKE and PBL acknowledge financial support from the Research Council of Norway. The computations presented in this paper were carried out on Titan, a cluster owned and maintained by the University of Oslo and NOTUR.

## APPENDIX

### PRECOMPUTING CONFIGURATION TABLES

In order to compute the two-and-three point functions, we have utilized the method introduced by Eriksen et al. (2004c).

The basic idea of this method is that given the resolution and the mask of the map, and the desired number of distance bins, the configurations that correspond to an angle  $\theta$  is uniquely determined. One may then do the work of finding these configurations only once, saving them in large tables. Each table then corresponds to a certain bin  $k$ , and

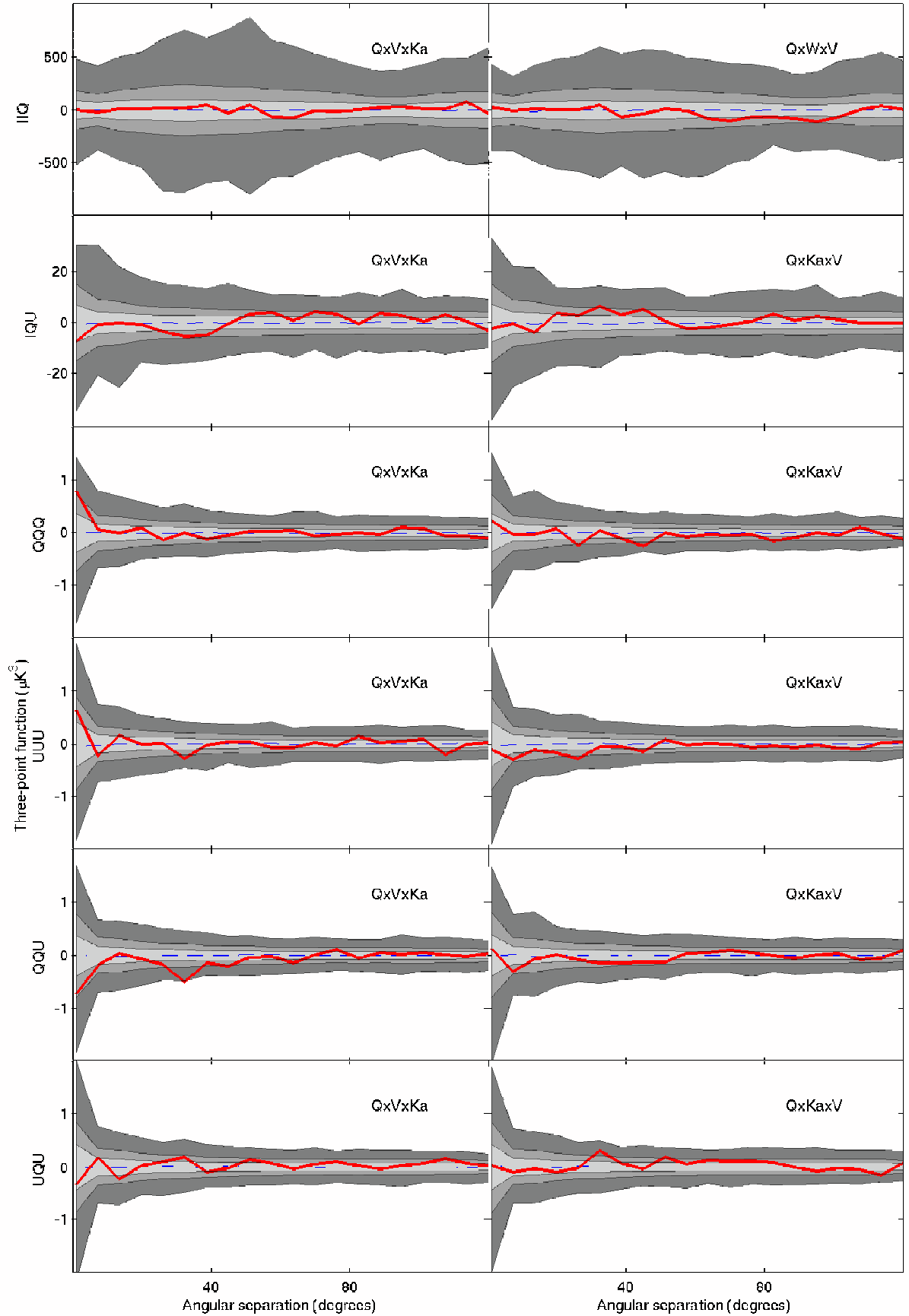


FIG. 5.— The equilateral three-point functions, computed with the KQ85 mask, as functions of angular separation on the sky. Only a representative selection is shown. The red line is the three-point function computed from the *WMAP* 5-year co-added maps. The light, medium and dark grey shaded areas correspond to  $1\sigma$ ,  $2\sigma$ , and  $3\sigma$ , respectively. The dashed blue line is the maximal point of the correlation histograms. Each row corresponds to a specific combination of modes, while the frequency bands involved are marked on each plot.

the first row in each table contains all the unmasked pixels of the map. Each column contains all pixels at a distance given by  $kd\theta$  from the pixel in the first element of the column. By moving through a column in such a table, one then traces out a circle of radius  $kd\theta$ . Thus, by saving the configurations in tables, one pays the initialization costs only once.

An additional, powerful feature of this approach becomes apparent when computing correlation functions of higher order than 2. If one thinks of these tables as compasses, tracing out circles of a given length for each pixel, it should be clear that, just as one can construct, e.g., triangles using compasses, one can construct triangles on the sphere using these tables. If the edges of the desired triangle is of lengths  $\theta$ ,  $\alpha$  and  $\beta$ , one begins with the  $\theta$  table, selects a pixel from the upper row, and selects a second pixel from the column below this pixel. One then has the base line of the triangle. To construct a triangle with a compass when the base line is given, one would adjust the compass so that it spans a length equal to the length of the second edge of the triangle, and draw a circle with this radius with one end of the base line as the center of the circle. Then, one would again adjust the compass so that it spans the desired third length of the triangle, and draw a circle around the other end of the base line. Then, one would check whether the two circles drawn intercept at any point(s). These points would then be the third vertex of the triangle. Carrying this analogy to our tables, our two already chosen pixels are the ends of the base line around which to draw our circles. We 'adjust our compass' by finding pixel 1 in the first row of table  $\alpha$ , we 'draw a circle around it' by looping over all pixels in the column below it, and do the same for pixel 2, expect that we now look in table  $\beta$ . By checking whether there are any common pixels in these 'circles', we find the triangle(s) whose edges have the desired lengths.

Since any  $N$ -point polygon can be reduced to triangles, higher order correlation functions can also be computed using this method.

#### REFERENCES

- Ashdown, M. A. J., et al. 2007, *A&A*, 467, 761  
 Bennett, C. L., et al. 1994, *ApJ*, 436, 423  
 Bennett, C. L., et al. 2003a, *ApJS*, 148, 1  
 Bennett, C. L., et al. 2003b, *ApJS*, 148, 97  
 Eriksen, H. K., Banday, A. J., & Górski, K. M. 2002, *A&A*, 395, 409  
 Eriksen, H. K., Hansen, F. K., Banday, A. J., Górski, K. M., & Lilje, P. B. 2004a, *ApJ*, 605, 14  
 Eriksen, H. K., Novikov, D. I., Lilje, P. B., Banday, A. J., & Górski, K. M. 2004b, *ApJ*, 612, 64  
 Eriksen, H. K., Lilje, P. B., Banday, A. J., & Górski, K. M. 2004c, *ApJS*, 151, 1  
 Eriksen, H. K., et al. 2004d, *ApJS*, 155, 227  
 Eriksen, H. K., Banday, A. J., Górski, K. M., & Lilje, P. B. 2005, *ApJ*, 622, 58  
 Eriksen, H. K., Huey, G., Banday, A. J., Górski, K. M., Jewell, J. B., O'Dwyer, I. J., & Wandelt, B. D. 2007, *ApJ*, 665, L1  
 Eriksen, H. K., Jewell, J. B., Dickinson, C., Banday, A. J., Górski, K. M., & Lawrence, C. R. 2008, *ApJ*, 676, 10  
 Górski, K. M. 1994, *ApJ*, 430, L85  
 Górski, K. M., Hivon, E., Banday, A. J., Wandelt, B. D., Hansen, F. K., Reinecke, M., Bartelman, M. 2005, *ApJ*, 622, 759  
 Hinshaw, G., et al. 1994, *ApJ*, 431, 1  
 Hinshaw, G., Banday, A. J., Bennett, C. L., Gorski, K. M., & Kogut, A. 1995, *ApJ*, 446, L67  
 Hinshaw, G., et al. 2003a, *ApJS*, 148, 135  
 Hinshaw, G., et al. 2003b, *ApJS*, 148, 63  
 Hinshaw, G., et al. 2007, *ApJS*, 170, 288  
 Hinshaw, G., et al. 2009, *ApJS*, 180, 225  
 Hivon, E., Górski, K. M., Netterfield, C. B., Crill, B. P., Prunet, S., & Hansen, F. 2002, *ApJ*, 567, 2  
 Jarosik, N., et al. 2003, *ApJS*, 148, 29  
 Kamionkowski, M., Kosowsky, A., & Stebbins, A. 1997, *Phys. Rev. D*, 55, 7368  
 Kogut, A., Banday, A. J., Bennett, C. L., Gorski, K. M., Hinshaw, G., Smoot, G. F., & Wright, E. L. 1996, *ApJ*, 464, L29  
 Kogut, A., et al. 2003, *ApJS*, 148, 161  
 Komatsu, E., et al. 2003, *ApJS*, 148, 119  
 Leach, S. M., et al. 2008, *A&A*, 491, 597  
 Lewis, A., & Bridle, S. 2002, *Phys. Rev. D*, 66, 103511  
 Smith, K. M. 2006, *Phys. Rev. D*, 74, 083002  
 Spergel, D. N., et al. 2003, *ApJS*, 148, 175  
 Verde, L., et al. 2003, *ApJS*, 148, 195  
 Zaldarriaga, M., & Seljak, U. 1997, *Phys. Rev. D*, 55, 1830